Journal of Biomedical Optics 8(2), 223–236 (April 2003)

Experimental validation of Monte Carlo modeling of fluorescence in tissues in the UV-visible spectrum

Quan Liu
University of Wisconsin-Madison
Department of Biomedical Engineering
Madison, Wisconsin 53706

Changfang Zhu
University of Wisconsin-Madison
Department of Electrical and Computer Engineering
Madison, Wisconsin 53706

Nirmala Ramanujam
University of Wisconsin-Madison
Department of Biomedical Engineering
1550 Engineering Drive, #2144
Madison, Wisconsin 53706
E-mail: nimmi@engr.wisc.edu

Abstract. The goal of the work is to experimentally verify Monte Carlo modeling of fluorescence and diffuse reflectance measurements in turbid, tissue phantom models. In particular, two series of simulations and experiments, in which one optical parameter (absorption or scattering coefficient) is varied while the other is fixed, are carried out to assess the effect of the absorption coefficient (μ_a) and scattering coefficient (μ_s) on the fluorescence and diffuse reflectance measured from a turbid medium. Moreover, simulations and experiments are carried out for several fiber optic probe geometries that are designed to sample small tissue volumes. Additionally, a group of conversion expressions are derived to convert the optical properties and fluorescence quantum yield measured from tissue phantoms for use in Monte Carlo simulations. The conversions account for the differences between the definitions of the absorption coefficient and fluorescence quantum yield of fluorophores in a tissue phantom model and those in a Monte Carlo simulation. The results indicate that there is good agreement between the simulated and experimentally measured results in most cases. This dataset can serve as a systematic validation of Monte Carlo modeling of fluorescent light propagation in tissues. The simulations are carried out for a wide range of absorption and scattering coefficients as well as ratios of scattering coefficient to absorption coefficient, and thus would be applicable to tissue optical properties over a wide wavelength range (UV-visible/near infrared). The fiber optic probe geometries that are modeled in this study include those commonly used for measuring fluorescence from tissues in practice.
 [DOI: 10.1117/1.1559057]

Keywords: Monte Carlo; fluorescence; diffuse reflectance; UV-visible; phantom; experimental validation.

Paper JBO-02044 received Jul. 15, 2002; accepted for publication Oct. 29, 2002.

1 Introduction

The Monte Carlo method has been developed to simulate light propagation in tissues for nearly two decades.[1] This computational modeling tool can provide insight into the design of experimental setups for optical measurements from human tissues, for understanding light distribution in human tissues, and for validation of analytical models of light transport. The parameters that can be modeled include illumination and collection geometries, three-dimensional light distribution in tissues, and different types of light-tissue interactions (for example, absorption, scattering, or fluorescence). These parameters can be simulated for a variety of tissue configurations (for example, homogeneous versus layered tissues) and optical properties. One of the important prerequisites to utilizing a Monte Carlo code is that it should be validated before use against a gold standard, such as a test dataset generated from an analytical model of light transport, or preferably, experimental measurements on tissue phantom models made up of a mixture of absorbers, scatterers, and fluorophores.

A number of groups have employed Monte Carlo modeling to simulate fluorescent light transport in tissues. A significant number of studies have been carried out to evaluate the effect of excitation and emission geometries, sample geometries, as well as absorption and scattering on tissue fluorescence.[2–10] To a lesser extent, Monte Carlo modeling has been employed to relate the bulk tissue fluorescence spectrum to the fluorescence originating from different layers within the tissue,[11–14] and for verification of analytical models of tissue fluorescence.[15–17]

Keijzer et al.[2] were perhaps the first group to simulate fluorescent light transport in turbid media using Monte Carlo modeling, and they showed that fluorescence spectra measured from turbid media depends on the geometry of excitation light delivery and emission light collection. Jianan et al.[3] used Monte Carlo simulations to identify appropriate illumination and collection geometries, at which the effect of optical properties on tissue fluorescence spectra could be minimized, and found that maximizing the overlap between illumination and collection areas minimizes the effect of absorption on the measured tissue fluorescence. Avriller et al.[6] used a fast Monte Carlo simulation to correct the distortion in tissue fluorescence spectra that arises from different separations between illumination and collection fibers. Pogue and Burke[9] used Monte Carlo simulations to show that if fluorescence is measured from a tissue volume, which is smaller than the average mean free-scattering path (inverse of the reduced scattering

1083-3668/2003/$15.00 © 2003 SPIE

coefficient), the effect of absorption will be further diminished. Pfefer et al.[8] examined the effect of optical fiber diameter, fiber-tissue spacing, and fiber numerical aperture on fluorescence spectroscopy using a single optical fiber probe. They observed that increasing the fiber diameter or fiber-tissue spacing increases the mean photon path length of collected fluorescent photons and produces a transition from a superficial to a deeper and more homogeneous probing volume in tissues. Increasing the numerical aperture results in an increase in fluorescence intensity, but the path lengths of collected fluorescent photons are not significantly affected for numerical apertures less than 0.8. Recently, Liu and Ramanujam[10] proposed the design of a variable aperture probe for depth-dependent fluorescence measurements from tissues. This study used Monte Carlo simulations to show that the fluorescence measured using completely overlapping illumination and collection apertures with variable diameters can be related to the depth of a fluorescent target (dysplastic region) in a turbid medium (epithelial tissue). Welch et al.[5] used Monte Carlo simulations to evaluate the effect of scattering, absorption, boundary conditions, geometry of the tissue sample, and the quantum yield of tissue fluorophores on the fluorescence spectrum measured from tissues, and showed that Monte Carlo modeling provides a realistic method for interpreting the effect of tissue sample geometries on the remitted fluorescence.

Although Monte Carlo modeling has been widely used to simulate the effect of illumination and collection geometries, sample geometries, and the effect of absorption and scattering on fluorescent light transport in tissues, the experimental validation of Monte Carlo simulations for fluorescent light propagation in turbid media has been carried out only to a limited extent.[9,17] Pogue and Burke[9] compared Monte Carlo simulations and experimental measurements of fluorescence as a function of fluorophore concentration in a turbid medium, measured with a 1-mm diameter fiber bundle composed of several fibers with a diameter of 100 μm. This was done for a low and a high absorption coefficient. Although they showed similar trends in both computational and experimental results, they did not carry out a quantitative comparison of the two approaches. Hyde et al.[17] compared the spatially resolved fluorescence obtained with Monte Carlo simulations to those obtained with diffusion theory and those obtained in phantom model experiments. Their results showed that the experimentally measured fluorescence is significantly higher than that predicted by theory (either Monte Carlo simulations or diffusion theory) at detector positions close to the source (1 mm), while they were in agreement at larger source-detector separations ($\sim$10 mm). In both studies, the simulations and experiments were accomplished at wavelengths where the scattering coefficient is significantly larger than the absorption coefficient.

Given an increasing interest in using Monte Carlo modeling to simulate fluorescent light transport in tissues for a range of optical properties and probe geometries, and the limited experimental validation of this technique, there is a need to perform systematic computational and experimental studies to validate Monte Carlo modeling of fluorescence in turbid media.

The goal of the work presented is to experimentally verify Monte Carlo modeling of fluorescence and diffuse reflectance measurements in turbid, tissue phantom models. In particular, simulations and experiments were carried out to assess the effect of the absorption coefficient (μ_a) and scattering coefficient (μ_s) on the fluorescence and diffuse reflectance measured from a turbid medium in the UV-visible spectrum, where scattering and absorption are comparable. Additionally, the simulations and experiments were carried out for several fiber optic probe geometries that are designed to sample small tissue volumes. The range of optical properties and sampling volumes investigated in this work complement those evaluated by Hyde et al.[17]

2 Materials and Methods

First, tissue phantom models with prescribed fluorescence excitation and emission characteristics, absorption and scattering properties and dimensions were prepared. Then, fluorescence and diffuse reflectance were experimentally measured from the phantom models over a range of absorption and scattering coefficients in the UV-visible spectrum and with several fiber optic probe geometries. Finally, the experimental results were compared to those obtained from Monte Carlo simulations of an equivalent theoretical model. A group of conversion expressions were derived to convert the optical properties and fluorescence quantum yield of tissue phantoms for use in the Monte Carlo simulations.

2.1 *Description of Tissue Phantoms*

The excitation-emission wavelength pair to be investigated was chosen to be (460, 520 nm). This wavelength pair falls within a spectral region, where the absorption coefficient of tissues is comparable to the scattering coefficient.[12,18] Furthermore, they are close to the excitation- emission maxima of two important fluorophores. One is flavin adenine dinucleotide (FAD), which is an endogenous fluorophore in tissue with an excitation-emission maximum of (450, 535 nm).[19] The other is a widely used molecular reporter of gene expression, green fluorescent protein (GFP), with an excitation-emission maximum near (460, 520 nm).[20] The optical properties of the phantom models at 460 and 520 nm were selected to be the representative of human epithelial tissues.[12,18] The absorption coefficient was varied from 1.3 to 31.8 cm^{-1}, and the scattering coefficient was varied from 50 to 225 cm^{-1}.

India ink (Super Black India Ink, The Speedball Art Products Company, Statesville, North Carolina) was chosen as the absorber since the ratio of its absorption coefficients at 460 and 520 nm is very similar to that of human epithelial tissues. The absorption coefficient of India ink, diluted by a factor of 1000 in distilled water, was measured using an absorption spectrophotometer (Cary 300, Varian, Australia) and quantified using Beer's law.

Figure 1 shows the absorption coefficient of pure India ink over the UV-visible spectrum. The absorption coefficient at a particular wavelength is linearly proportional to the concentration of India ink according to Beer's law, which greatly facilitates the calculation of appropriate concentrations for a particular absorption coefficient. To achieve a desired absorption coefficient in the phantom model, pure India ink was diluted by an appropriate dilution factor, and the absorption coefficient of the final concentration was verified again using the absorption spectrophotometer.

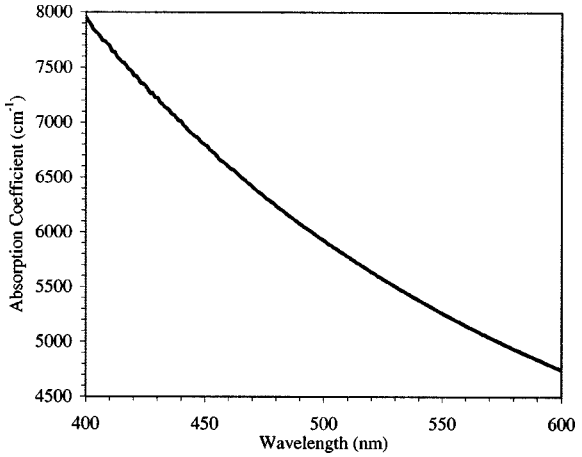

Fig. 1 Absorption coefficient of pure India ink over the UV-visible spectrum.

Polystyrene spheres with a diameter of 1.053 μm and a refractive index of 1.6 (Polysciences Incorporated, Warrington, Pennsylvania) were chosen as the scatterer because they have a uniform and well-characterized particle size distribution, as well as low absorption and fluorescence at the excitation and emission wavelengths employed in this study. According to Durkin, Jaikumar, and Richards-Kortum,[21] the absorption coefficient of 0.625% polystyrene spheres with a diameter of 1.05 μm and a refractive index of 1.56 is about 0.50 cm^{-1} at wavelengths between 400 and 600 nm. The wavelength-dependent scattering coefficient of a specific fractional volume of polystyrene spheres, with a known diameter and refractive index, was predicted by use of the Mie theory.[22] These calculations were verified by comparing our results to experimentally measured values in the publication by Durkin, Jaikumar, and Richards-Kortum.[21]

Figure 2 shows the scattering coefficient of polystyrene spheres suspended in distilled water with a fractional volume of 2.6%, 1.053-μm diameter and a refractive index of 1.6 over the UV-visible spectrum. The scattering coefficient of polystyrene spheres is linearly proportional to its concentration for the concentration used and wavelength ranges of interest according to our calculations, which greatly facilitates the calculation of appropriate concentrations of the suspension for a particular scattering coefficient. To achieve a desired scattering coefficient in the phantom model, the fractional volume of polystyrene spheres was diluted by an appropriate dilution factor.

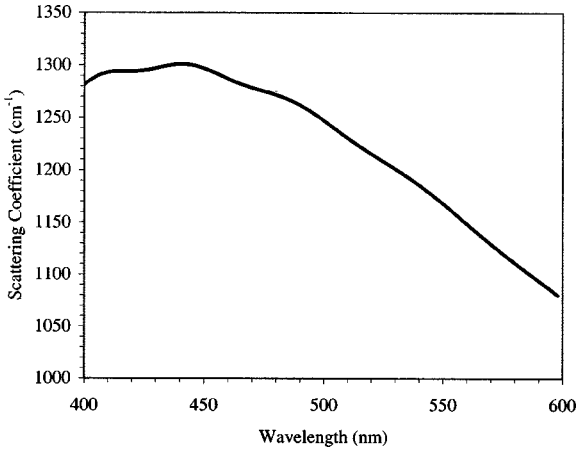

Fig. 2 Scattering coefficient of polystyrene spheres with a fractional volume of 2.6% in distilled water, 1.053-μm diameter, and refractive index of 1.6 over the UV-visible spectrum.

The fluorophore used in the tissue phantom experiments was FAD, which is one of the endogenous fluorophores present in human epithelial tissues as mentioned previously. The concentration of FAD to be used in the tissue phantoms was selected to be such that its absorption coefficient is at least one order of magnitude lower than the smallest absorption coefficient contributed by India ink in the tissue phantom models at both the excitation and emission wavelengths. The absorption coefficient spectrum of FAD in distilled water was measured at various concentrations using the absorption spectrophotometer. A concentration of 7-μM FAD yielded an absorption coefficient of 0.108 cm^{-1} at 460 nm, and 0.001 cm^{-1} at 520 nm, which are at least one order of magnitude lower than the lowest absorption coefficient of India ink ($\sim$1.2 cm^{-1}) in the tissue phantom model at both the excitation and emission wavelengths. Therefore, the concentration of FAD in all the phantom models was fixed at 7 μM.

Two sets of tissue phantoms were prepared for the experimental measurements of fluorescence and diffuse reflectance. In the first set of phantoms (group 1), the scattering coefficient and fluorophore concentration were fixed at 110.4 cm^{-1} and 7 μM, respectively, while the absorption coefficient was varied from 1.204 to 31.704 cm^{-1}. In the second set of phantoms (group 2), the absorption coefficient and the fluorophore concentration were fixed at 10.709 cm^{-1} and 7 μM, respectively, and the scattering coefficient was varied from 50 to 225 cm^{-1}. Tables 1 and 2 show the concentrations of each component and corresponding optical properties in tissue phantom groups 1 and 2, respectively. It should be noted that all the phantoms contained 7-μM FAD.

After the optical properties of interest were established, the lateral and depth dimensions of the tissue phantom models were determined. Specifically, a Monte Carlo simulation was carried out for a homogeneous semi-infinite medium, in which the optical properties were set to be the smallest absorption coefficient (1.2 cm^{-1}) and largest scattering coefficient (225 cm^{-1}) employed in the tissue phantom models. These optical properties were chosen to maximize the fluence distribution in the medium. The dimensions of the medium were increased until the photon interactions with boundaries were negligible. A diameter of 1 cm and a depth of 0.5 cm were determined to be the minimum required dimensions of tissue phantom models.

Cylindrical plastic bottles with a height of 5 cm and a diameter of 2 cm (Plastic Snap Cap Vial, distributed by Fisher Scientific) were used as containers for the phantoms. The phantoms were filled up to a height of 3 cm in the containers. A diameter of 2 cm and a depth of 3 cm were sufficient to meet the requirements of a semi-infinite homogeneous medium as determined previously.

Table 1 Concentrations of each component and corresponding optical properties of tissue phantom group 1 with variable absorption coefficients (μ_a), fixed scattering coefficient (μ_s), anisotropy factor (g), and fluorophore concentration (7-μM FAD).

India ink ($\times 10^{-2}$ ml/10 ml)	2.6% Polystyrene sphere suspension (ml/10 ml)	μ_a (cm^{-1}), μ_s (cm^{-1}), g at 460 nm	μ_a (cm^{-1}), μ_s (cm^{-1}), g at 520 nm
0.2462	0.8579	1.204, 110.4, 0.926	0.994, 104.3, 0.926
0.4924	0.8579	1.917, 110.4, 0.926	1.596, 104.3, 0.926
0.9849	0.8579	5.178, 110.4, 0.926	4.352, 104.3, 0.926
1.9698	0.8579	10.208, 110.4, 0.926	8.580, 104.3, 0.926
2.9546	0.8579	14.319, 110.4, 0.926	12.012, 104.3, 0.926
3.9395	0.8579	19.083, 110.4, 0.926	16.043, 104.3, 0.926
4.9244	0.8579	21.128, 110.4, 0.926	17.754, 104.3, 0.926
5.9093	0.8579	31.704, 110.4, 0.926	26.517, 104.3, 0.926

2.2 *Instruments and Fiber Optic Probes for Fluorescence and Diffuse Reflectance Measurements*

Three types of fluorometers with three different kinds of fiber optic probes were used in this study. Figure 3 shows the cross-sectional views of the common ends of three fiber optic probes employed to measure the fluorescence, and in most cases the diffuse reflectance, of the tissue phantom models. The filled area represents the illumination fiber(s) and the unfilled area represents the collection fiber(s). It should be noted that the collection fibers in Fig. 3(c) are round, although they appear slightly elliptical. The configuration of illumination and collection fibers in each fiber optic probe and a description of the corresponding instruments are provided next.

The first instrument (Fluorolog-3, J.Y. Horiba Incorporated, New Jersey) incorporates a 450-W Xenon lamp, a photomultiplier tube (PMT), and double excitation and emission scanning monochromators. The corresponding fiber optic probe (a) [see Fig. 3(a)] has a central illumination fiber with a core/cladding diameter of 200/245 μm, surrounded by a concentric ring composed of nine collection fibers, each with a core/cladding diameter of 100/130 μm. The distance between the center of the illumination fiber and the center of each collection fiber is 187.5 μm. The numerical aperture (NA) of all fibers is 0.22.

The second instrument (Skinscan, J.Y. Horiba Incorporated, New Jersey) comprises a 150-W Xenon lamp, a PMT, and double excitation and emission scanning monochromators. The corresponding fiber optic probe (b) [see Fig. 3(b)] has a collection core with a diameter of 1.52 mm surrounded by an illumination ring, with an outer diameter of 2.18 mm. Both the illumination ring and collection core are composed of 31 individual fibers, each with a core/cladding diameter of 200/245 μm. This fiber optic probe differs from the one described previously with respect to the illumination and collection geometries (here the outer ring is used for illumination and the central core for collection, while in the previous probe

Table 2 Concentrations of each component and corresponding optical properties of tissue phantom group 2 with variable scattering coefficients (μ_s), fixed absorption coefficient (μ_a), anisotropy factor (g), and fluorophore concentration (7-μM FAD).

India ink ($\times 10^{-2}$ ml/10 ml)	2.6% Polystyrene sphere suspension (ml/10 ml)	μ_a (cm^{-1}), μ_s (cm^{-1}), g at 460 nm	μ_a(cm^{-1}), μ_s(cm^{-1}), g at 520 nm
1.9698	0.3886	10.709, 50.0, 0.926	9.007, 47.2, 0.926
1.9698	0.5828	10.709, 75.0, 0.926	9.007, 70.8, 0.926
1.9698	0.7771	10.709, 100.0, 0.926	9.007, 94.4, 0.926
1.9698	0.9714	10.709, 125.0, 0.926	9.007, 118.0, 0.926
1.9698	1.1656	10.709, 150.0, 0.926	9.007, 141.6, 0.926
1.9698	1.3599	10.709, 175.0, 0.926	9.007, 165.3, 0.926
1.9698	1.5542	10.709, 200.0, 0.926	9.007, 188.9, 0.926
1.9698	1.7485	10.709, 225.0, 0.926	9.007, 212.5, 0.926

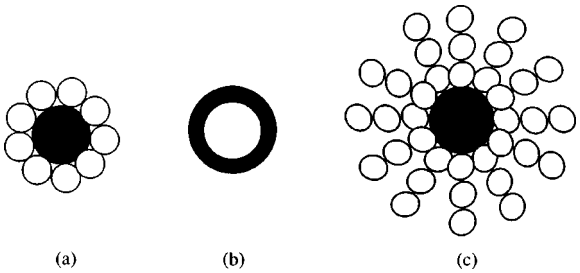

Fig. 3 Cross-section views of the common ends of three fiber optic probes employed to measure the fluorescence, and in most cases the diffuse reflectance, of the tissue phantom models. The filled area represents the illumination fiber(s) and the unfilled area represents the collection fiber(s). Note that the collection fibers in (c) are round, although they appear slightly elliptical.

the central fiber is used for illumination and the surrounding ring for collection) and the effective illumination and collection areas.

The third custom-built instrument consists of a 450-W xenon lamp (FL-1039, J.Y. Horiba Incorporated, New Jersey) coupled to a scanning double excitation monochromator (Gemini 180, J.Y. Horiba Incorporated, New Jersey), a filter wheel, an imaging spectrograph (Triax 320, J.Y. Horiba Incorporated, New Jersey) and a CCD camera (CCD 3000, J.Y. Horiba Incorporated, New Jersey). The common end of the corresponding fiber optic probe (c) [see Fig. 3(c)] consists of an illumination core with a 1180 μm diameter (made up of 19 fibers, each with a core/cladding diameter of 200/245 μm), and three surrounding concentric rings of collection fibers (each ring has 12 fibers and each fiber has a core/cladding diameter of 200/245 μm). The NA of all fibers is 0.22. The output of the three concentric rings of collection fibers on the CCD chip can be spatially separated, thereby allowing for optical spectroscopic measurements to be made at three source-detector separations simultaneously. This fiber optic probe design is similar to that described in Fig. 3(a), in that both of them consist of a central illumination core surrounded by one or several concentric rings of collection fibers. However, the illumination core here is much larger than that used previously, and there are three collection rings instead of one in this fiber optic probe. The distances between collection rings and the geometrical center of the probe are 735, 980, and 1225 μm, respectively, and these separations are much larger than that in the fiber optic probe shown in Fig. 3(a).

Table 3 provides the integration time and the excitation and emission bandpasses for fluorescence and diffuse reflectance measurements with each fiber optic probe and corresponding instrument. The procedure of the measurement is the same for all instruments and fiber optic probes and are described as follows. The fluorescence measurements were made at an excitation-emission wavelength pair of (460, 520 nm) and the diffuse reflectance was measured at 460 nm. The background fluorescence of each tissue phantom (containing the absorber and scatterer only) was measured before the addition of the fluorophore FAD. Then the fluorescence and diffuse reflectance of each phantom was measured after the addition of FAD. Each measurement was performed three times. The dark current of the instrument was measured prior to the diffuse reflectance measurements. The background fluorescence was subtracted from the experimental fluorescence measurement, and the dark current was subtracted from the experimental diffuse reflectance measurement. In the end, the three background-subtracted fluorescence measurements and the three dark current-subtracted diffuse reflectance measurements were averaged. During the course of the measurements, the probes were immersed a few millimeters into the phantoms to ensure that there was no air gap between the probe tip and the phantoms. The phantoms were stirred during the course of each experimental measurement to prevent polystyrene spheres from settling down at the bottom of containers.

2.3 *Monte Carlo Simulations*

2.3.1 *General Parameters*

A three-dimensional, weighted-photon Monte Carlo code (written in standard C)[23] was modified to simulate fluorescence.[24] The original code was used for diffuse reflectance simulations. Up to five million photons were launched in each simulation at random uniformly distributed locations over a range of angles defined by an NA of 0.22 and over a circular or ring-like illumination area at the top surface of the medium. In the case of fluorescence simulations, a rejection scheme was used to determine whether or not the absorbed

Table 3 Integration time and the excitation and emission bandpasses for fluorescence and diffuse reflectance measurements with each fiber optic probe and corresponding instrument.

Fiber optic probe	Instrument	Integration time (s)	Excitation bandpass (nm)	Emission bandpass (nm)
(a)	Fluorolog-3 (fluorescence measurement only)	5	5	10
(b)	Skinscan (fluorescence and reflectance measurements)	5	5	5
(c)	Custom-built instrument (fluorescence measurement)	5	12.39	10.56
(c)	Custom-built instrument (reflectance measurement)	1.4	1.77	10.56

fraction of a photon packet is emitted as a fluorescent photon. The fluorescence or diffuse reflectance escaping the medium was collected over a circular area defined by the collection diameter and an NA of 0.22. The refractive index of the medium above the model was set to 1.452 to simulate an optical fiber, and that below the model was set to 1.0. A cylindrical coordinate system, in which the axial dimension is perpendicular to the top surface of the medium and the radial dimension corresponds to any direction perpendicular to the axial dimension, was applied to track the photons' path and record quantities of interest. The axial and radial grid sizes were both 0.01 cm. In the simulations, the photons travel in a semi-infinite medium, but the scored quantities are recorded only in the region of interest. The region of interest was set to a volume with a thickness of 0.5 cm and a diameter of 1 cm (which corresponds to a total of 50 axial and 50 radial grids).

To simulate fluorescence and diffuse reflectance measurements with fiber optic probe (a) [see Fig. 3 (a) for the cross-sectional view], the illumination diameter was set at 200 μm. One collection fiber with a diameter of 100 μm was used. Although the actual fiber optic probe has nine collection fibers, the comparison of the simulations to the experimental measurements was not affected, because it is the profiles of the normalized fluorescence/reflectance versus absorption/scattering coefficients, rather than the absolute intensities, that would be compared. The center-to-center distance was set to be 187.5 μm. In the case of the fiber optic probe (b) [see Fig. 3 (b) for the cross-sectional view], photons were incident over a ring area, which is defined by an inner diameter of 1.52 mm and an outer diameter of 2.18 mm. All the photons exiting within a circular area defined by an inner diameter of 1.52 mm and a cone defined by an NA of 0.22 were collected. In the case of a fiber optic probe (c) [see Fig. 3(c) for the cross-sectional view], the illumination area was defined by a diameter of 1180 μm, which was obtained by calculating the distance from the geometrical center of the fiber bundle to the outer edge of the outermost illumination fiber. Three collection fibers were used, each with a diameter of 200 μm and at different distances from the center of the illumination area. The three center-to-center distances were 735, 980, and 1225 μm.

For each simulation, one million [for fiber optic probe (a)] up to five million [for fiber optic probes (b) and (c)] photons were launched to ensure the convergence of results. The number of photons was increased for the simulations of fluorescence measurements with fiber optic probes (b) and (c) to account for the significantly larger illumination areas of the latter two probe geometries. The quantum yield of all phantoms was set to be 1 during the simulations to ensure that sufficient fluorescence photons were detected. After the simulation, the collected fluorescence was scaled to match the actual quantum yield of the corresponding tissue phantom model, which is explained in more detail in the following section. Simulations were run on several Sun-Ultra-5_10 machines with a SUNOS-5.8 operating system and 512 Mbyte RAM. The running time ranged from several hours to several days.

2.3.2 *Conversion of Experimental Optical Properties and Quantum Yield of Phantom Models for Monte Carlo Simulations*

In the tissue phantom model studies, the absorber and fluorophore have two distinct absorption coefficients, both of which contribute to the total absorption coefficient of the phantom. In the Monte Carlo simulations, however, the absorber and fluorophore are usually described by one combined absorption coefficient. To compare the experimental results to the simulation results, the independent absorption coefficients of the absorber and fluorophore in the tissue phantom model have to be converted to a combined absorption coefficient for use in the Monte Carlo simulations. Moreover, the quantum yield of the fluorophore in the tissue phantom has to be rescaled for the Monte Carlo simulations. The following section shows the derivation of the conversion equations that yield the combined absorption coefficient and scaled quantum yield of the tissue phantom models for use in the Monte Carlo simulations.

Expressions for absorption, scattering, and fluorescence in a tissue phantom model.

Consider a tissue phantom model that consists of an absorber with an absorption coefficient of μ_a, a scatterer with a scattering coefficient of μ_s, and a fluorophore with an absorption coefficient of μ_{af} and a quantum yield of ϕ.

For a photon with unit energy that is undergoing an attenuation event (absorption or scattering), its energy has three possible fates.

1. The probability that the photon is absorbed by the absorber can be defined as:
$$\frac{\mu_a}{\mu_a+\mu_{af}+\mu_s}. \tag{1}$$
2. The probability that the photon is absorbed by the fluorophore can be defined as:
$$\frac{\mu_{af}}{\mu_a+\mu_{af}+\mu_s}. \tag{2}$$
This possibility can be further subdivided into two categories.
   a. The probability that the absorbed photon is converted to fluorescence is ϕ; thus the probability of the photon being absorbed by the fluorophore and converted to fluorescence is:
$$\frac{\mu_{af}}{\mu_a+\mu_{af}+\mu_s}\cdot\phi. \tag{3}$$
   b. The probability that the absorbed photon is not converted to fluorescence is $1-\phi$, thus the probability of the photon being absorbed by the fluorophore but not converted to fluorescence is:
$$\frac{\mu_{af}}{\mu_a+\mu_{af}+\mu_s}\cdot(1-\phi), \tag{4}$$
3. The probability of the photon being scattered by the scatterer is:
$$\frac{\mu_s}{\mu_a+\mu_{af}+\mu_s}. \tag{5}$$

In summary, the probability that the photon is absorbed (by either the absorber or fluorophore) without fluorescing is obtained by adding expressions (1) and (4):

$$\frac{\mu_a}{\mu_a+\mu_{af}+\mu_s}+\frac{\mu_{af}}{\mu_a+\mu_{af}+\mu_s}\cdot(1-\phi)=\frac{\mu_a+\mu_{af}\cdot(1-\phi)}{\mu_a+\mu_{af}+\mu_s}. \quad (6)$$

The probability that the photon is converted to fluorescence is equivalent to expression (3):

$$\frac{\mu_{af}\cdot\phi}{\mu_a+\mu_{af}+\mu_s}. \quad (7)$$

The probability that the photon is scattered by the scatterer is equivalent to expression (5):

$$\frac{\mu_s}{\mu_a+\mu_{af}+\mu_s}. \quad (8)$$

Expressions for absorption, scattering, and fluorescence in the Monte Carlo model.

In the Monte Carlo simulations, the absorption coefficient of the absorber and fluorophore are described by a single combined absorption coefficient μ_{ac}. The probabilities shown in expressions (6) to (8) are rewritten next for the combined absorption coefficient μ_{ac}, scattering coefficient μ_{sc}, and quantum yield ϕ_c.

1. The probability that the photon is absorbed by either the absorber or fluorophore without generating fluorescence is:
$$\frac{\mu_{ac}\cdot(1-\phi_c)}{\mu_{ac}+\mu_{sc}}. \quad (9)$$
2. The probability that the photon is converted to fluorescence is:
$$\frac{\mu_{ac}\cdot\phi_c}{\mu_{ac}+\mu_{sc}}. \quad (10)$$
3. The probability that the photon is scattered by the scatterer is:
$$\frac{\mu_{sc}}{\mu_{ac}+\mu_{sc}}. \quad (11)$$

Conversion expressions.

To express the optical properties and quantum yield in tissue phantoms as a combined set of optical properties and rescaled quantum yield, respectively, for Monte Carlo modeling, the following equations need to be equivalent to each other.

Expression (6) must equal expression (9):

$$\frac{\mu_a+\mu_{af}\cdot(1-\phi)}{\mu_a+\mu_{af}+\mu_s}=\frac{\mu_{ac}\cdot(1-\phi_c)}{\mu_{ac}+\mu_{sc}}. \quad (12)$$

Expression (7) must equal expression (10):

$$\frac{\mu_{af}\cdot\phi}{\mu_a+\mu_{af}+\mu_s}=\frac{\mu_{ac}\cdot\phi_c}{\mu_{ac}+\mu_{sc}}. \quad (13)$$

Expression (8) must equal expression (11):

$$\frac{\mu_s}{\mu_a+\mu_{af}+\mu_s}=\frac{\mu_{sc}}{\mu_{ac}+\mu_{sc}}. \quad (14)$$

Solving this group of equations yields the following expressions:

$$\mu_{ac}=\mu_a+\mu_{af}, \quad (15)$$

$$\phi_c=\frac{\mu_{af}\cdot\phi}{\mu_a+\mu_{af}}, \quad (16)$$

$$\mu_{sc}=\mu_s. \quad (17)$$

Note that the scattering coefficient is not affected by conversion in Eq. (17). Equation (15) can be used to convert the absorption coefficient contributed separately by the fluorophore and the absorber in the tissue phantom into a combined absorption coefficient, and Eq. (16) can be used to scale the quantum yield used in the Monte Carlo simulations. Tables 4 and 5 show the combined optical properties and scaled quantum yields of tissue phantom groups 1 and 2, respectively for use in the Monte Carlo simulations.

Table 4 Variable absorption coefficients (μ_a), fixed scattering coefficient (μ_s), anisotropy factor (g), and quantum yield of tissue phantom group 1 (see Table 1) for use in the Monte Carlo simulations.

μ_a (cm^{-1}), μ_s (cm^{-1}), g and quantum yield at 460 nm	μ_a (cm^{-1}), μ_s (cm^{-1}), g at 520 nm
1.312, 110.4, 0.926, 0.762	0.994, 104.3, 0.926
2.025, 110.4, 0.926, 0.494	1.596, 104.3, 0.926
5.286, 110.4, 0.926, 0.189	4.352, 104.3, 0.926
10.316, 110.4, 0.926, 0.097	8.580, 104.3, 0.926
14.427, 110.4, 0.926, 0.069	12.012, 104.3, 0.926
19.191, 110.4, 0.926, 0.052	16.043, 104.3, 0.926
21.236, 110.4, 0.926, 0.047	17.754, 104.3, 0.926
31.812, 110.4, 0.926, 0.031	26.517, 104.3, 0.926

3 Results

3.1 *Results for Fiber Optic Probe Geometry (a)*

Figure 4 shows the fluorescence measured from a tissue phantom groups 1 and (b) tissue phantom group 2 with fiber optic probe geometry (a) [see Fig. 3(a)] and the corresponding Monte Carlo simulation results. The number closest to each data point in Fig. 4(a) is the absorption coefficient at the excitation wavelength (460 nm), and the number closest to each data point in Fig. 4(b) is the scattering coefficient at the excitation wavelength (the same format has been used in Figs. 5 through 9). The absorption and scattering coefficients at the

Table 5 Variable scattering coefficients (μ_s), fixed absorption coefficient (μ_a), anisotropy factor (g), and quantum yield of tissue phantom group 2 (see Table 2) for use in the Monte Carlo simulations.

μ_a(cm^{-1}), μ_s(cm^{-1}), g, and quantum yield at 460 nm	μ_a (cm^{-1}), μ_s (cm^{-1}), g at 520 nm
10.817, 50.0, 0.926, 1	9.007, 47.2, 0.926
10.817, 75.0, 0.926, 1	9.007, 70.8, 0.926
10.817, 100.0, 0.926, 1	9.007, 94.4, 0.926
10.817, 125.0, 0.926, 1	9.007, 118.0, 0.926
10.817, 150.0, 0.926, 1	9.007, 141.6, 0.926
10.817, 175.0, 0.926, 1	9.007, 165.3, 0.926
10.817, 200.0, 0.926, 1	9.007, 188.9, 0.926
10.817, 225.0, 0.926, 1	9.007, 212.5, 0.926

emission wavelength (520 nm) are lower than those at the excitation wavelength by 16% and 6%, respectively, for all data points. Each experimental data point has been normalized by the sum of all experimental data points, and each simulation data point has also been normalized by the sum of all simulation data points. This method of normalization sets the area under the curve to unity and facilitates comparison between the computational and experimental results. The error bar represents variation in three consecutive measurements from each phantom, which is too small to be clearly observed at most points.

Figure 4(a) indicates that the fluorescence intensity decreases with an increase in the absorption coefficient. The percent error was calculated for each data point. and it is defined as the ratio of the difference between computational and experimental values (numerator) to the experimental value (denominator). and then multiplied by a factor of 100. The lowest percent error is 0.3% (for $\mu_a = 14.427$ cm^{-1}) and the highest is 14.4% (for $\mu_a = 21.236$ cm^{-1}). Figure 4(b) shows that the fluorescence intensity increases as the scattering coefficient is increased. The lowest percent error is 0.1% (for $\mu_s = 125$ cm^{-1}) and the maximum percent error is 6.0% (for $\mu_s = 75$ cm^{-1}). There is good agreement between the computational and experimental results over the range of absorption and scattering coefficients employed in these phantom studies.

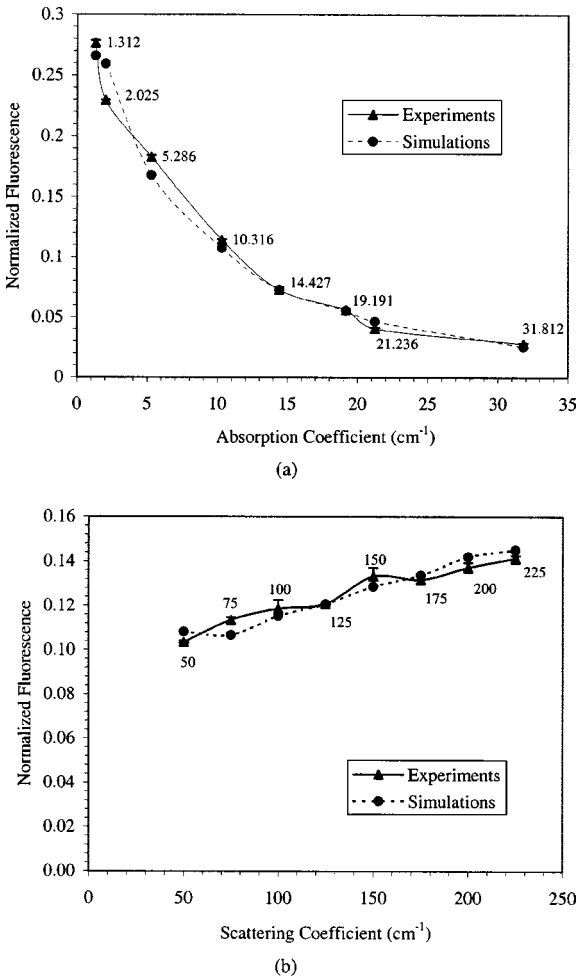

Fig. 4 Fluorescence measured from tissue phantom group 1 and tissue phantom group 2 with fiber optic probe geometry (a) [see Fig. 3(a)] and the corresponding Monte Carlo simulation results. The number closest to each data point in Fig. 4(a) is the absorption coefficient at the excitation wavelength of 460 nm, and the number closest to each data point in Fig. 4(b) is the scattering coefficient at the excitation wavelength. The absorption and scattering coefficients at the emission wavelength (520 nm) are lower than that at the excitation wavelength by 16 and 6%, respectively, for all data points. Each experimental data point has been normalized by the sum of all experimental data points, and each simulation data point has also been normalized by the sum of all simulation data points. The error bar represents the variation in three consecutive measurements from each phantom.

3.2 *Results for Fiber Optic Probe Geometry (b)*

Figure 5 shows the normalized fluorescence measured from (a) tissue phantom group 1 and (b) tissue phantom group 2 with fiber optic probe geometry (b) [see Fig. 3(b)] and the corresponding Monte Carlo simulation results. The trends shown in the normalized fluorescence in Figs. 5(a) and 5(b) are similar to those observed in Fig. 4(a) and 4(b), respectively. In Fig. 5(a), the lowest percent error is 1.1% (for $\mu_a = 14.427$ cm^{-1}), and the highest is 28.6% (for $\mu_a = 21.236$ cm^{-1}). In Fig. 5(b), the lowest percent error is 0.02% (for $\mu_s = 225$ cm^{-1}), and the maximum error is 8.1% (for $\mu_s = 50$ cm^{-1}). The percent errors observed for this probe geometry are greater than those observed for fiber optic probe geometry (a).

Figure 6 shows the normalized diffuse reflectance measured from tissue phantom group 1 and tissue phantom group 2 with fiber optic probe geometry (b) [see Fig. 3(b)] and the corresponding Monte Carlo simulation results. Both curves have been normalized in the same manner as described previously. The trends in the diffuse reflectance measurements are similar to those observed in the fluorescence measurements. In Fig. 6(a), the lowest percent error is 3.3% (for $\mu_a = 1.312$ cm^{-1}), and the highest is 22.4% (for $\mu_a = 19.191$ cm^{-1}), excluding the last data point. At the last data point, the percent error is 49.2% (for $\mu_a = 31.812$ cm^{-1}), but the signal inten-

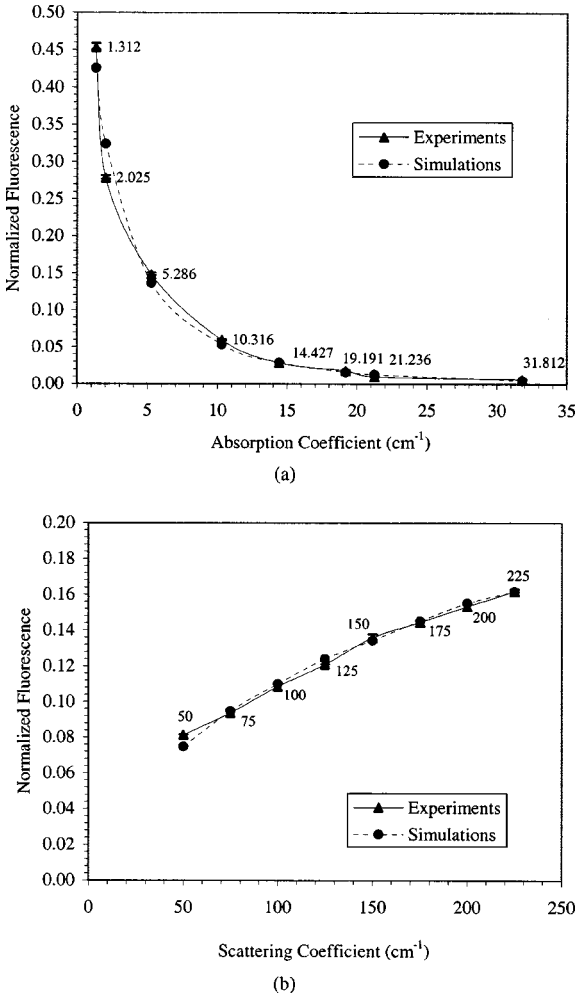

Fig. 5 Normalized fluorescence measured from tissue phantom group 1 and tissue phantom group 2 with fiber optic probe geometry (b) [see Fig. 3(b)] and corresponding Monte Carlo simulation results. The number closest to each data point in Fig. 5(a) is the absorption coefficient at the excitation wavelength of 460 nm, and the number closest to each data point in Fig. 5(b) is the scattering coefficient at the excitation wavelength. Each experimental data point has been normalized by the sum of all experimental data points, and each simulation data point has also been normalized by the sum of all simulation data points. The error bar represents the variation in three consecutive measurements from each phantom.

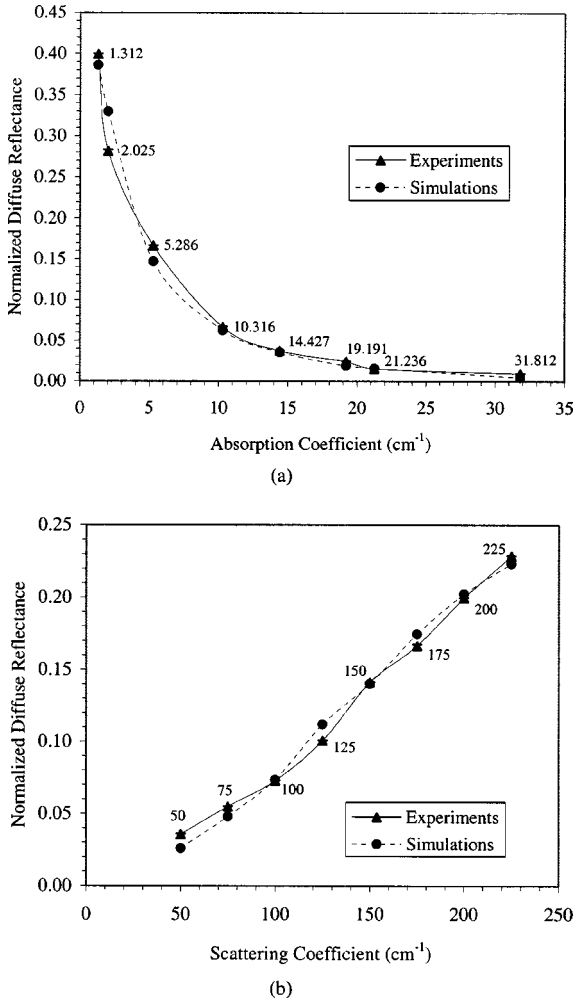

Fig. 6 Normalized diffuse reflectance measured from tissue phantom group 1 and tissue phantom group 2 with fiber optic probe geometry (b) [see Fig. 3(b)] and corresponding Monte Carlo simulation results. The number closest to each data point in Fig. 6(a) is the absorption coefficient at an excitation wavelength of 460 nm, and the number closest to each data point in Fig. 6(b) is the scattering coefficient at the excitation wavelength. Each experimental data point has been normalized by the sum of all experimental data points, and each simulation data point has also been normalized by the sum of all simulation data points. The error bar represents the variation in three consecutive measurements from each phantom.

sity at this point is too small to be reliable. In Fig. 6(b), the lowest percent error is 0.67% (for $\mu_s = 150$ cm^{-1}), and the maximum percent error is 27.5% (for $\mu_s = 50$ cm^{-1}). The percent error for the diffuse reflectance data is higher than that for the fluorescence data obtained using the same fiber optic probe.

3.3 *Results for Fiber Optic Probe Geometry (c)*

In the previous results it can be seen that the agreement between the computational and experimental results is significantly better for tissue phantom group 2, where the scattering coefficient is varied, than that for tissue phantom group 1. Furthermore, these results do not significantly depend on the fiber optic probe geometry. Thus, in the remaining section, only the results corresponding to tissue phantom group 1 are presented.

Figure 7 shows the normalized fluorescence measured from tissue phantom group 1 with fiber optic probe geometry (c) [see Fig. 3(c)] and corresponding Monte Carlo simulation results. Fiber optic probe (c) contains three independent collection fiber rings with different distances relative to the geometrical center of the illumination core. Thus, there are three pairs of curves in this figure, which correspond to the fluorescence collected by the (a) inner, (b) middle, and (c) outer rings, respectively. The trends of the fluorescence in Figs. 7(a), 7(b), and 7(c) are similar to those seen in Figs. 4(a) and 5(a). In Fig. 7(a), the lowest percent error is 2.0% (for $\mu_a = 5.286$ cm^{-1}), and the highest is 20.4% (for $\mu_a = 31.812$

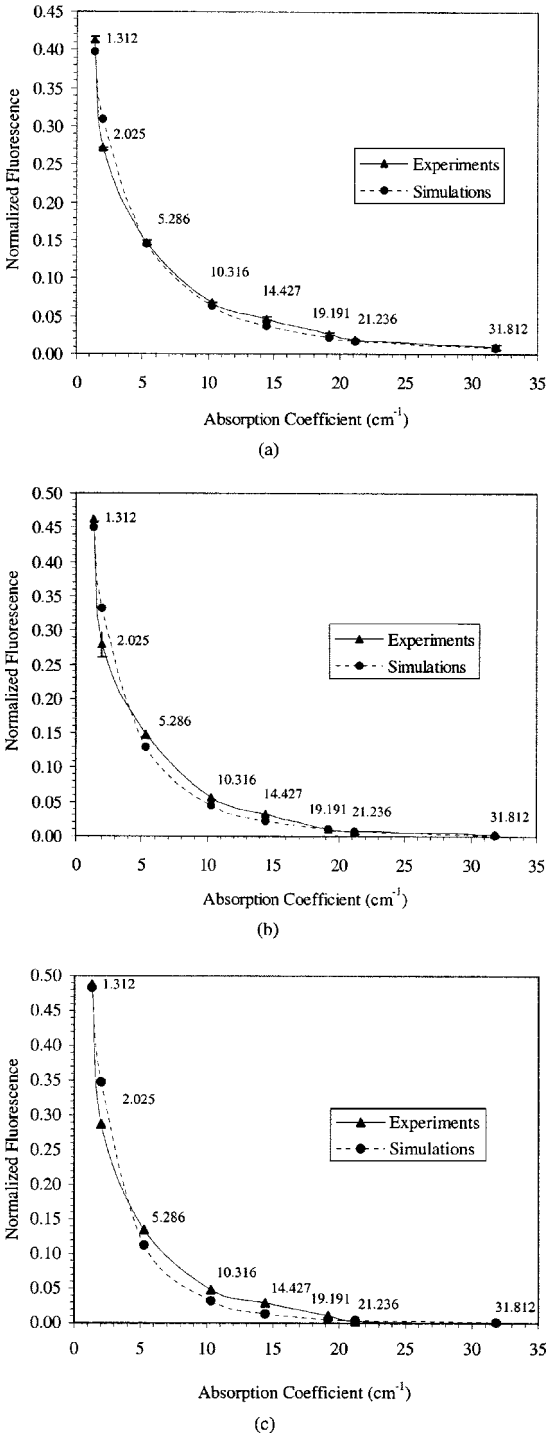

Fig. 7 Normalized fluorescence measured from tissue phantom group 1 with fiber optic probe geometry (c) [see Fig. 3(c)] and the corresponding Monte Carlo simulation results. Fiber optic probe (c) contains three independent collection fiber rings with different distances relative to the geometrical center of the illumination core, thus there are three pairs of curves in this figure, which correspond to the fluorescence collected by (a) inner, (b) middle, and (c) outer rings, respectively. The number closest to each data point is the corresponding absorption coefficient at the excitation wavelength of 460 nm. Each experimental data point has been normalized by the sum of all experimental data points, and each simulation data point has also been normalized by the sum of all simulation data points. The error bar represents the variation in three consecutive experimental measurements from each phantom.

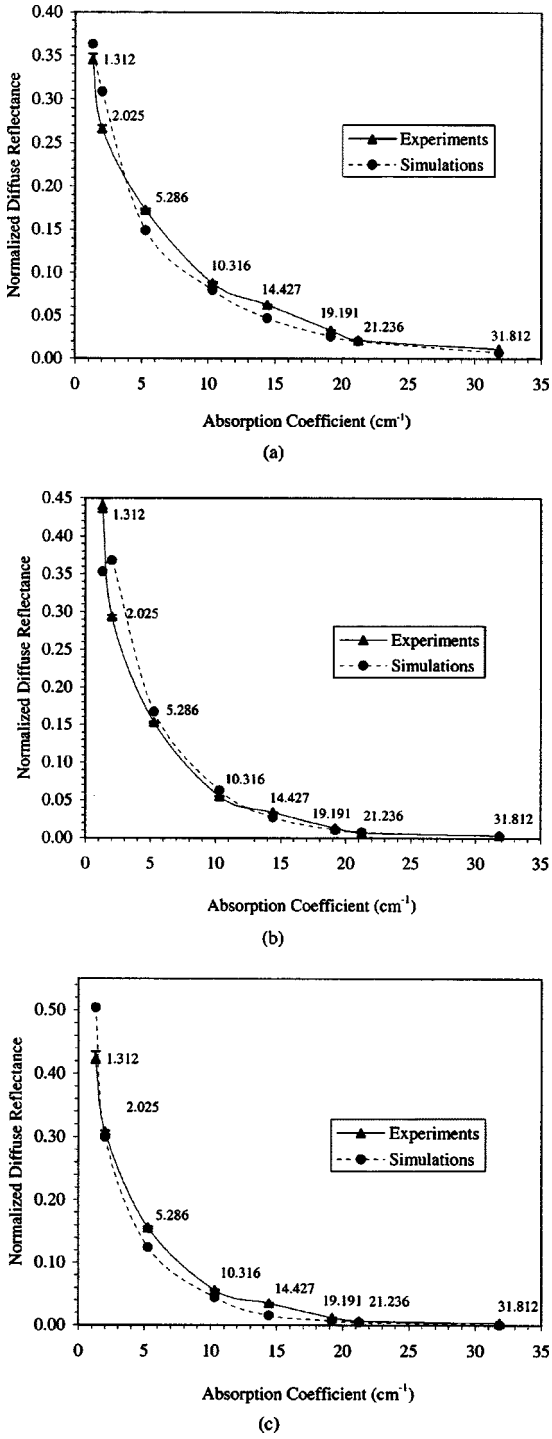

Fig. 8 Normalized diffuse reflectance measured from tissue phantom group 1 with fiber optic probe geometry (c) [see Fig. 3(c)] and the corresponding Monte Carlo simulation results. Fiber optic probe (c) contains three independent collection fiber rings with different distances relative to the geometrical center of the illumination core, thus there are three pairs of curves in this figure, which correspond to the diffuse reflectance collected by the (a) inner, (b) middle, and (c) outer rings, respectively. The number closest to each data point is the corresponding absorption coefficient at an excitation wavelength of 460 nm. Each experimental data point has been normalized by the sum of all experimental data points, and each simulation data point has also been normalized by the sum of all simulation data points. The error bar represents the variation in three consecutive experimental measurements from each phantom.

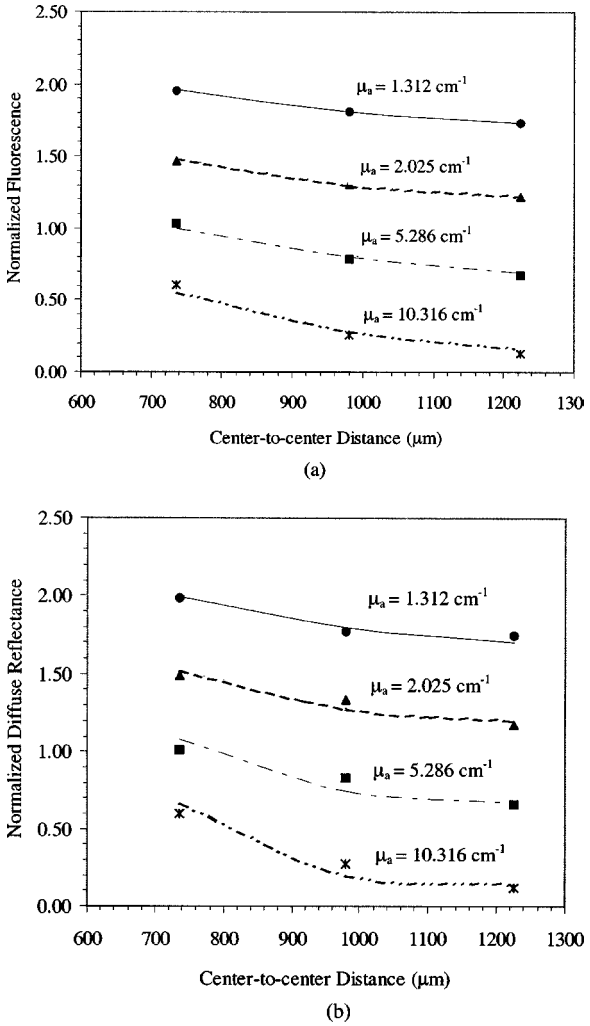

Fig. 9 Radial distribution of the normalized (a) fluorescence and (b) diffuse reflectance measured from tissue phantom group 1 with fiber optic probe geometry (c) [Fig. 3(c)] and the corresponding Monte Carlo simulation results. The three center-to-center distances are 735, 980, and 1225 μm, respectively, which correspond to the distance from the center of the inner, middle, and outer collection rings, respectively, to the center of fiber optic probe (c). The fluorescence/diffuse reflectance radial profiles are shown only for the cases of the four smallest absorption coefficients in tissue phantom group 1. The absorption coefficient corresponding to that at wavelength 460 nm is indicated above the corresponding data points. The data points for simulation results are denoted by individual markers. The three experimentally obtained data points have been interpolated and connected by smoothed curves to facilitate comparison between the computational and experimental results and also to easily distinguish them. The curves are spaced out on the *y* axis for clarity. Each data point has been normalized by the sum of all three data points in the same dataset.

cm^{-1}). In Fig. 7(b), the lowest percent error is 2.6% (for $\mu_a = 1.312\ cm^{-1}$), and the highest percent error is 42.4% (for $\mu_a = 31.812\ cm^{-1}$). In Fig. 7(c), the lowest percent error is 0.7% (for $\mu_a = 1.312\ cm^{-1}$), and the highest error is 54.8% (for $\mu_a = 14.427\ cm^{-1}$). The percent errors observed for the inner collection ring [Fig. 7(a)] are comparable to those observed for fiber optic probes (a) and (b). However, the percent errors for the middle and outer collection rings [Figs. 7(b) and 7(c)] are significantly greater than those observed for fiber optic probes (a) and (b).

Figure 8 shows the normalized diffuse reflectance measured from tissue phantom group 1 with fiber optic probe geometry (c) [see Fig. 3(c)] and corresponding Monte Carlo simulation results. The diffuse reflectance curves shown in Figs. 8(a), 8(b), and 8(c) display similar trends with those observed in Fig. 6(a). In Fig. 8(a), the lowest percent error is 5.3% (for $\mu_a = 1.312\ cm^{-1}$), and the highest is 39.5% (for $\mu_a = 31.812\ cm^{-1}$). In Fig. 8(b), the lowest percent error is 5.4% (for $\mu_a = 21.236\ cm^{-1}$), and the maximum error is 25.2% (for $\mu_a = 2.025\ cm^{-1}$). Moreover, the simulated data at $\mu_a = 1.312\ cm^{-1}$ is believed to be a random error, since the diffuse reflectance intensity at this point is expected to be greater than that at $\mu_a = 2.025\ cm^{-1}$. In Fig. 8(c), the lowest percent error is 2.6% (for $\mu_a = 2.025\ cm^{-1}$), and the maximum percent error is 32.9% (for $\mu_a = 31.812\ cm^{-1}$). The percent errors observed here are greater than those observed for diffuse reflectance measurements with fiber optic probe (b), and are also greater than those of the corresponding fluorescence results obtained with the same fiber optic probe geometry.

Figure 9 shows the radial distribution of the normalized fluorescence and diffuse reflectance measured from tissue phantom group 1 with fiber optic probe geometry (c) [see Fig. 3(c)] and corresponding Monte Carlo simulation results. The three center-to-center distances are 735, 980, and 1225 μm, respectively, which correspond to the distance from the center of the inner, middle, and outer collection rings, respectively to the center of fiber optic probe (c). The fluorescence/diffuse reflectance radial profiles are shown only for the four smallest absorption coefficients of tissue phantom group 1. The absorption coefficient corresponding to that at the excitation wavelength 460 nm is indicated on top of each curve. The curves are spaced out on the *y* axis for clarity. Each data point within a curve has been normalized by the sum of all three data points. In addition, the three experimentally obtained data points on each curve have been interpolated and connected by a curve to facilitate comparison between the computational and experimental results. The fluorescence and diffuse reflectance decrease with increasing center-to-center distance. The percent error increases as the absorption coefficient increases. As observed previously, the fluorescence data show better agreement between the computational and experimental results compared to the diffuse reflectance data.

3.4 *Summary of Minimum/Maximum Percent Error Between Computational and Experimental Results*

Table 6 summarizes the minimum/maximum percent errors and corresponding optical properties (at an excitation wavelength of 460 nm) for the normalized fluorescence data obtained from tissue phantom group 1 and tissue phantom group 2. In Table 6, the maximum percent error increases from fiber optic probe (a), to probe (b), to probe (c). Furthermore, the maximum percent error increases as the center-to-center distance is increased in fiber optic probe (c). In general, the maximum percent error occurs at absorption coefficient values greater than 20 cm^{-1}. In Table 7, the maximum percent error occurs at scattering coefficient values smaller than 75 cm^{-1}. The maximum percent errors are greater between the

Table 6 The minimum/maximum percent errors and corresponding optical properties (at an excitation wavelength of 460 nm) for the normalized fluorescence data obtained from tissue phantom group 1. The last data point for the outer ring for probe (c) was excluded when considering the maximum percent error because the signal at this point was too small to be reliable.

			Probe (c)		
	Probe (a)	Probe (b)	Inner ring	Middle ring	Outer ring
Minimum percent error (%)	0.3	1.1	2.0	2.6	0.7
μ_a (cm^{-1}) at minimum	14.427	14.427	5.286	1.312	1.312
Maximum percent error (%)	14.4	28.6	20.4	42.4	54.8
μ_a (cm^{-1}) at maximum	21.236	21.236	31.812	31.812	14.427

computational and experimental results for tissue phantom group 1 (see Table 6) compared to those for tissue phantom group 2 (see Table 7).

Table 8 and 9 summarizes the minimum/maximum percent errors and corresponding optical properties (at the wavelength 460 nm) for the normalized diffuse reflectance obtained from tissue phantom group 1 and tissue phantom group 2. In general, the trends observed for the normalized diffuse reflectance data are similar to those observed for the normalized fluorescence data, with the exception at the middle collection ring of fiber optic probe (see Table 8).

4 Discussion

The computational and experimental results show that both the fluorescence and diffuse reflectance decrease with an increase in the absorption coefficient and an increase in the distance between illumination and collection fibers due to the increased attenuation of excitation and emission light in the medium. In contrast, both the fluorescence and diffuse reflectance increase gradually with an increase in the scattering coefficient. The reason is that increasing the scattering coefficient widens the excitation light distribution in the tissue volume. This in turn gives rise to a broader distribution of fluorescent light. Thus, both the excitation photons and fluorescent photons are more likely to be detected by the distant collection fibers as the scattering coefficient is increased.

The computational and experimental fluorescence results show the best agreement in the case of fiber optic probe geometry (a). The percent error between the simulation and experimental results progressively increases as the illumination and collection geometry is changed from probe (a), to probe (b) to probe (c). This could be attributed in part to how well the Monte Carlo modeling method can reproduce the experimental fiber optic probe geometries. Fiber optic probe (a), which has a single illumination fiber and one ring of collection fibers, is relatively straightforward to simulate. However, the second, and particularly the third, fiber optic probes have a more complicated illumination and collection fiber bundle configuration. In fiber optic probe (b), the illumination ring and the collection core each contain 31 fibers. These fibers are not exactly uniformly distributed throughout the illumination ring or collection core, thus resulting in an inhomogeneous illumination and collection area. Similar imperfections are present in the illumination core of fiber optic probe (c). Thus, the effective illumination and collection areas of fiber optic probes (b) and (c) are more difficult to be exactly simulated in the Monte Carlo model.

Table 7 The minimum/maximum percent errors and corresponding optical properties (at an excitation wavelength of 460 nm) for the normalized fluorescence data obtained from tissue phantom group 2.

	Probe (a)	Probe (b)
Minimum percent error (%)	0.1	0.02
μ_s (cm^{-1}) at minimum	125	225
Maximum percent error (%)	6.0	8.1
μ_s (cm^{-1}) at maximum	75	50

The disparity between the computational and experimental fluorescence results in the case of fiber optic probes (b) and (c) may also be attributed to increased illumination and collection areas of these probes compared to those of fiber optic probe (a). The larger the illumination and collection areas, the lower the photon density (photons delivered to or collected from the top surface of the model per unit area) will be in the Monte Carlo simulations. The number of photons launched per unit area for fiber optic probes (b) and (c) was lower than that for fiber optic probe (a) by a factor of 12 and 6, respectively. Therefore, a larger number of incident photons may be required to obtain an accurate result. However, it was computationally prohibitive to increase the number of photons to be much greater than 5 million in our simulations. Another potential source of error in the case of fiber optic probe (c) can be the relatively larger center-to-center distance between the illumination and collection fibers, which will further decrease the number of detected photons. These findings suggest that a decrease in the number of incident/collected photons will increase the error in the simulation results. This could be easily tested for specific cases where the errors are large, thus providing a rule of thumb for the number of photons to launch in a simulation for a given set of tissue optical properties and probe parameters. However, this is beyond the scope of the current study.

Table 8 The minimum/maximum percent errors and corresponding optical properties (at an excitation wavelength of 460 nm) for the normalized diffuse reflectance obtained from tissue phantom group 1. The last data point for probe (b) was excluded when considering the maximum percent error because the signal at this point was too small to be reliable.

		Probe (c)		
	Probe (b)	Inner ring	Middle ring	Outer ring
Minimum percent error (%)	3.3	5.3	5.4	2.6
μ_a (cm^{-1}) at minimum	1.312	1.312	21.236	2.025
Maximum percent error (%)	22.4	39.5	25.2	82.9
μ_a (cm^{-1}) at maximum	19.191	31.812	2.025	31.812

Another observation is that the maximum percent error in the fluorescence and diffuse reflectance measurements often occurs at a point where the absorption coefficient is relatively large ($\mu_a > 20\ cm^{-1}$) and/or the scattering coefficient is relatively small ($\mu_s < 75\ cm^{-1}$). All of these points correspond to relatively small signals, thus a small signal-to-noise ratio. Therefore, the measurement uncertainties due to the small signal-to-noise ratio may also contribute to the disparities between the simulated and experimental data.

An interesting finding is that the agreement between the computational and experimental fluorescence results is better than that observed for the diffuse reflectance results [except for the case of the middle collection ring in fiber optic probe (c)]. A possible reason is that both the absorption coefficient and scattering coefficient of phantoms at the emission wavelength are smaller than those at the excitation wavelength, which results in a longer mean free path of a photon at the emission wavelength compared to that at the excitation wavelength. (Note: mean free path $l = 1/\mu_a + \mu_s$ is the measure of the distance that a photon can travel freely in a medium without interaction with the medium.) A longer mean free path means that less steps are required to travel an equal distance, which enables a fluorescent photon (at the emission wavelength) to travel from the originating site to the collection fiber in a shorter path, in comparison to an excitation photon that has a shorter mean free path. A photon traveling a shorter path will be less affected by the optical properties of a medium, and thus will be less affected by the deviations between the actual optical properties of the tissue phantoms and the optical properties used in the Monte Carlo simulations. Therefore, the simulation of fluorescent photons, i.e., fluorescence, will be less affected by the errors in the optical properties than that of the excitation photons, i.e., diffuse reflectance.

Table 9 The minimum/maximum percent errors and corresponding optical properties (at an excitation wavelength of 460 nm) for the normalized diffuse reflectance obtained from tissue phantom group 2.

	Probe (b)
Minimum percent error (%)	0.67
μ_s (cm^{-1}) at minimum	150
Maximum percent error (%)	27.5
μ_s (cm^{-1}) at maximum	50

The imperfect phantom models may also contribute to the disagreement between the experimental and simulation results. Polystyrene spheres are small latex particles suspended in water. Since these spheres have a higher density than water, they tend to settle down in quiescence. In our experiments, a stirring bar was used to keep the polystyrene spheres in suspension. The turbulence in the solution caused by stirring may contribute to deviations in the experimental results. It is also important to note that the scattering coefficient of polystyrene spheres was calculated using the Mie theory. Although the accuracy of our Mie code was verified by comparing our test results to that obtained experimentally by Durkin, Jaikumar, and Richards-Kortum,[21] the results for this specific application were not experimentally quantified. Additionally, it was assumed that the refractive index of the polystyrene spheres is the same at the excitation and emission wavelengths for the Mie theory calculations. Potential errors due to stirring and prediction of the scattering coefficients could cause slight disparities between the experimental and simulation results.

In summary, this study compares both fluorescence and diffuse reflectance data, measured experimentally from tissue phantom models to those obtained from Monte Carlo simulations for different absorption and scattering coefficients, and for several different fiber optic probe geometries. The results indicate that there is good agreement between the simulated and measured results in most cases. This dataset serves as a systematic validation of Monte Carlo modeling of fluorescent light transport in tissues. The simulations were carried out for a wide range of absorption and scattering coefficients and the ratios of scattering coefficient to absorption coefficient, and thus would be applicable to tissue optical properties over a wide wavelength range (UV-visible/near infrared). The fiber optic probe geometries that are modeled in this study include those commonly used to measure fluorescence from tissues. Monte Carlo codes developed by other researchers can be compared to the simulation datasets provided here to verify the accuracy of their numerical schemes. In addition, when comparisons are made between Monte Carlo simulations (using a code with a structure similar to that described in this

study) and experimental measurements from tissue phantom studies, the conversion Eqs. (15) through (17) derived in the Methods section have to be applied to the optical properties of the experimental phantom models to get the proper input optical properties for the Monte Carlo simulations.

Acknowledgments

The authors would like to acknowledge support from the Prize University Fellowship from the University of Wisconsin-Madison (Q. Liu) and the Whitaker Foundation (N. Ramanujam). In addition, the authors would like to acknowledge the contributions of Amit Nimunkar and Dina Hagl during the early stage of this work.

References

1. B. C. Wilson and G. Adam, ''A Monte Carlo model for the absorption and flux distributions of light in tissue,'' *Med. Phys.* **10**, 824–830 (1983).
2. M. Keijzer, R. R Richards Kortum, S. L. Jacques, and M. S. Feld, ''Fluorescence spectroscopy of turbid media: autofluorescence of the human aorta,'' *Appl. Opt.* **28**, 4286–4292 (1989).
3. J. Qu, C. MacAulay, S. Lam, and B. Palcic, ''Laser-induced fluorescence spectroscopy at endoscopy: tissue optics, Monte Carlo modeling, and in vivo measurements,'' *Opt. Eng.* **34**, 3334–3343 (1995).
4. B. W. Pogue and T. Hasan, ''Fluorophore quantitation in tissue- simulating media with confocal detection,'' *IEEE J. Sel. Top. Quantum Electron.* **2**, 959–964 (1996).
5. A. J. Welch, C. Gardner, R. Richards-Kortum, E. Chan, G. Criswell, J. Pfefer, and S. Warren, ''Propagation of fluorescent light,'' *Lasers Surg. Med.* **21**, 166–178 (1997).
6. S. Avrillier, E. Tinet, D. Ettori, J. M. Tualle, and B. Gelebart, ''Influence of the emission-reception geometry in laser-induced fluorescence spectra from turbid media,'' *Appl. Opt.* **37**, 2781–2787 (1998).
7. J. Y. Qu, Z. Huang, and H. Jianwen, ''Excitation-and-collection geometry insensitive fluorescence imaging of tissue-simulating turbid media,'' *Appl. Opt.* **39**, 3344–3356 (2000).
8. T. J. Pfefer, K. T. Schomacker, M. N. Ediger, and N. S. Nishioka, ''Light propagation in tissue during fluorescence spectroscopy with single-fiber probes,'' *IEEE J. Sel. Top. Quantum Electron.* **7**, 1004–1012 (2001).
9. B. W. Pogue and G. Burke, ''Fiber-optic bundle design for quantitative fluorescence measurement from tissue,'' *Appl. Opt.* **37**, 7429–7436 (1998).
10. Q. Liu and N. Ramanujam, ''Relationship between depth of a target in a turbid medium and fluorescence measured by a variable-aperture method,'' *Opt. Lett.* **27**, 104–106 (2002).
11. H. Zeng, C. MacAulay, D. I. McLean, and B. Palcic, ''Reconstruction of in vivo skin autofluorescence spectrum from microscopic properties by Monte Carlo simulation,'' *J. Photochem. Photobiol., B* **38**, 234–240 (1997).
12. G. I. Zonios, R. M. Cothren, J. T. Arendt, W. Jun, J. Van Dam, J. M. Crawford, R. Manoharan, and M. S. Feld, ''Morphological model of human colon tissue fluorescence,'' *IEEE Trans. Biomed. Eng.* **43**, 113–122 (1996).
13. R. Drezek, K. Sokolov, U. Utzinger, I. Boiko, A. Malpica, M. Follen, and R. Richards-Kortum, ''Understanding the contributions of NADH and collagen to cervical tissue fluorescence spectra: modeling, measurements, and implications,'' *J. Biomed. Opt.* **6**, 385–396 (2001).
14. W. Zheng, Z. Huang, S. Xie, B. Li, S. M. Krishnan, and T. C. Chia, ''Autofluorescence spectrum of human bronchial tissue by Monte Carlo modelling,'' *Acta-Photonica-Sinica* **30**, 669–674 (2001).
15. J. Wu, M. S. Feld, and R. P. Rava, ''Analytical model for extracting intrinsic fluorescence from a turbid media,'' *Appl. Opt.* **32**, 3585–3595 (1993).
16. M. G. Muller, I. Georgakoudi, Z. Qingguo, W. Jun, and M. S. Feld, ''Intrinsic fluorescence spectroscopy in turbid media: disentangling effects of scattering and absorption,'' *Appl. Opt.* **40**, 4633–4646 (2001).
17. D. E. Hyde, T. J. Farrell, M. S. Patterson, and B. C. Wilson, ''A diffusion theory model of spatially resolved fluorescence from depth-dependent fluorophore concentrations,'' *Phys. Med. Biol.* **46**, 369–383 (2001).
18. R. Marchesini, E. Pignoli, S. Tomatis, S. Fumagalli, A. E. Sichirollo, S. Di Palma, M. Dal Fante, P. Spinelli, A. C. Croce, and G. Bottiroli, ''Ex vivo optical properties of human colon tissue,'' *Lasers Surg. Med.* **15**, 351–357 (1994).
19. B. Chance, B. Schoener, R. Oshino, F. Itshak, and Y. Nakase, ''Oxidation-reduction ratio studies of mitochondria in freeze-trapped samples. NADH and flavoprotein fluorescence signals,'' *J. Biol. Chem.* **254**, 4764–4771 (1979).
20. A. B. Cubitt, R. Heim, S. R. Adams, A. E. Boyd, L. A. Gross, and R. Y. Tsien, ''Understanding, improving and using green fluorescent proteins,'' *Trends Biochem. Sci.* **20**, 448–455 (1995).
21. A. J. Durkin, S. Jaikumar, and R. Richards-Kortum, ''Optically dilute, absorbing and turbid phantoms for fluorescence spectroscopy of homogeneous and inhomogeneous samples,'' *Appl. Spectrosc.* **47**, 6829 (1994).
22. F. C. Bohren and R. D. Huffman, *Absorption and Scattering of Light by Small Particles*, John Wiley & Sons, Inc., New York (1983).
23. W. Lihong, S. L. Jacques, and Z. Liqiong, ''MCML-Monte Carlo modeling of light transport in multi-layered tissues,'' *Comput. Methods Programs Biomed.* **47**, 131–146 (1995).
24. M. J. McShane, S. Rastegar, M. Pishko, and G. L. Cote, ''Monte Carlo modeling for implantable fluorescent analyte sensors,'' *IEEE Trans. Biomed. Eng.* **47**, 624–632 (2000).